Journal of Energy Storage 66 (2023) 107396

Contents lists available at ScienceDirect

Journal of Energy Storage

journal homepage: www.elsevier.com/locate/est

Research papers

Three-dimensional hierarchically porous micro sponge-ball comprising anatase TiO_2 nanodots and nitrogen-doped graphitic carbon as anodes for ultra-stable lithium-ion batteries

Jae Seob Lee [a,b,1], Hye Seon Ka [a,1], Rakesh Saroha [a], Yun Chan Kang [b], Dong-Won Kang [c,*], Jung Sang Cho [a,*]

[a] Department of Engineering Chemistry, Chungbuk National University, Chungbuk 361-763, Republic of Korea
[b] Department of Materials Science and Engineering, Korea University, Anam-Dong, Seongbuk-Gu, Seoul 136-713, Republic of Korea
[c] School of Energy Systems Engineering, Chung-Ang University, Seoul 06974, Republic of Korea

ARTICLE INFO

Keywords:
Spray pyrolysis
Three-dimensional micro sponge-ball
Nitrogen-doped carbon
Titanium dioxide anode
lithium-ion batteries

ABSTRACT

Hierarchically porous three-dimensional micro sponge-balls comprising highly conductive nitrogen-doped graphitic carbon (NGC) and anatase-type TiO_2 nanodots (TiO_2@NGC MSB) are synthesized using spray pyrolysis technique followed by heat treatment. The as-sprayed powders obtained after spray pyrolysis consist of polystyrene (PS) nanobeads-derived macropores and anatase TiO_2 nanodots embedded in an amorphous carbon (AC)-NGC carbon matrix (TiO_2@NGC-AC MSB). The subsequent heat treatment of the as-sprayed powders at 300 °C resulted in the formation of additional micropores by selective removal of the AC into gaseous products to form TiO_2@NGC MSB. The obtained hierarchically porous and highly conductive architecture guarantees effective electrolyte infiltration inside the electrode, enhanced Li-ion diffusion, and faster charge transfer during the redox reactions. Benefited from the structural merits, the TiO_2@NGC MSB anode exhibits remarkable electrochemical performance compared to those of TiO_2@NGC-AC MSB and filled-type TiO_2 anodes. A reasonable discharge capacity of 105 mA h g^{-1} at a high current density of 10.0 A g^{-1} and exceptional cycling performance (219 mA h g^{-1} with 0.0006 % decay rate after 2000 cycles at 2.0 A g^{-1} and 160 mA h g^{-1} with 0.003 % decay rate after 5000 cycles at 3.0 A g^{-1}) are obtained.

1. Introduction

Titanium-based oxides, such as spinel-type lithium titanate ($Li_4Ti_5O_{12}$) and titanium dioxide (TiO_2), have been explored intensively as promising anodes for high-performance lithium-ion batteries (LIBs) [1–4]. In particular, anatase-type TiO_2 (white) is considered a more reasonable anode than commercially available graphitic anodes owing to its high theoretical capacity [335 mA h g^{-1}, which is almost twice that of $Li_4Ti_5O_{12}$ (175 mA h g^{-1})], natural abundance, nontoxicity, and high safety [5–11]. In addition, it undergoes a low volume expansion (<4 %) during redox reactions compared to commercial graphite (~10 %), thus exhibiting excellent cycling stability and structural integrity [12–17]. Moreover, the solid-electrolyte interphase (SEI) formed in the case of commercial graphite at 0.8 V vs. Li^+/Li is highly unstable, particularly at normal battery operation conditions (< 100 °C) and undergoes an exothermic reaction, leading to safety issues [18,19]. Furthermore, the three-dimensional crystal structure of anatase TiO_2 facilitates faster Li-ion insertion and extraction [15]. However, anatase TiO_2 allows only

Abbreviations: MSB, micro sponge-balls; NGC, nitrogen-doped graphitic carbon; PS, polystyrene; AC, amorphous carbon; LIBs, lithium-ion batteries; SEI, solid-electrolyte interphase; TTIP, titanium(IV) isopropoxide; PVP, polyvinylpyrrolidone; F-TiO_2, filled TiO_2; FE-SEM, field-emission scanning electron microscopy; FE-TEM, field-emission transmission electron microscopy; HR-TEM, high-resolution transmission electron microscopy; TGA, thermogravimetric analysis; BET, Brunauer–Emmett–Teller; XPS, X-ray photoelectron spectroscopy; EA, elemental analysis; FEC, fluoroethylene carbonate; DMC, dimethyl carbonate; CV, cyclic voltammetry; EIS, electrochemical impedance spectroscopy; SAED, selected area electron diffraction; ICEs, initial Coulombic efficiencies; R_s, solution resistance; R_{ct}, charge transfer resistance.

* Corresponding authors.
E-mail addresses: kangdwn@cau.ac.kr (D.-W. Kang), jscho@cbnu.ac.kr (J.S. Cho).
[1] These authors contributed equally to this work.

https://doi.org/10.1016/j.est.2023.107396
Received 24 January 2023; Received in revised form 20 March 2023; Accepted 9 April 2023
Available online 26 April 2023

0.5 mol of Li-ions into half of the octahedral sites available (a total of four) in a single TiO_2 unit cell, resulting in a theoretical discharge capacity of 175 mA h g^{-1} [20,21]. Additionally, due to its high operating voltage window (1.0–3.0 V), the practical energy density of a Li-ion cell employing anatase TiO_2 as the anode is considerably lower than that of a Li-ion cell utilizing graphite as the negative electrode. Furthermore, owing to its high energy bandgap (~3.2 eV), the anatase TiO_2 anode exhibits high internal resistance and structural defects caused by repeated Li-ion insertion/extraction, which subsequently hinders the reaction kinetics [22].

To address these issues, various strategies have been employed, including the development of novel materials design with unique morphologies, such as fiber-in-tube [3], porous nanofibers [12], multichannel hollow structures [23], nanowires [24], nanotubes [25], doping with different atoms [26,27], different phases [28,29], carbon composites [30,31], and several more [32]. Several research groups have previously used porous TiO_2 microspheres for various applications, such as microwave absorption [33], photocatalysis [34], and sensing applications [35]. Similarly, the porous structure is highly preferred for energy storage applications as it not only allows efficient electrolyte infiltration inside the electrode but also channelizes unwanted volume variations, thus resulting in an overall improved electrochemical performance. For instance, Wang et al. synthesized multi-shelled TiO_2 hollow microspheres using a sacrificial method that controlled the shell thickness, number of shells, and intershell spacing [36]. The resulting nanostructure exhibited improved rate and cycling performance (119 mA h g^{-1} at 10.0C after 1200 cycles). Similarly, Gao et al. prepared mesoporous polyaniline/anatase-type TiO_2 microspheres with a core-shell structure using a hydrothermal technique and reported a reasonable rate performance [37].

Another crucial factor that guarantees enhanced electrochemical performance is the presence of a highly conductive carbon matrix, particularly nitrogen-doped graphitic carbon (NGC). Nitrogen doping enhances the electrical conductivity ofwing to the high electronegativity of the nitrogen than that of carbon [38,39]. Yin et al. reported a carbon-coated TiO_2 nanocomposite as an anode for LIBs, in which carbon decoration was performed using a resorcinol-formaldehyde solution through the sol-gel process [40]. The nanostructure exhibited a high-rate performance (up to 10.0C) and reasonable cycling stability (171 mA h g^{-1} after 330 cycles at 2.0C). However, the synergistic effect of the hierarchical porous structure and selectively controlled highly conductive carbon skeleton has been rarely examined and therefore needs to be investigated thoroughly. The synergistic effect of the intentionally chosen wide operating voltage range (0.001–3.0 V) was also discussed in detail. To the best of our knowledge, a three-dimensional nanostructure that resembles a sponge-ball comprising evenly distributed macropores and highly conductive NGC matrix/anatase-type TiO_2 nanodots as high-performance anodes has not been reported to date.

Inspired by the above discussion, a facile spray pyrolysis method followed by a heat-treatment step was adopted to prepare a three-dimensional hierarchically porous micro sponge-ball comprising NGC and anatase-type TiO_2 nanodots (TiO_2@NGC MSB) as high-performance anodes for LIBs. The heat treatment process at 300 °C facilitated the selective removal of amorphous carbon (AC) species from gaseous products and the formation of micropores, thus enhancing the overall electrical conductivity and porosity of the sample. Additionally, macropores were generated throughout the internal and external structures using a polystyrene (PS) nanobead solution as a porogen with a diameter of 100 nm. The TiO_2@NGC MSB anode exhibited high-rate performance and excellent cycling stability owing to the structural advancements. Furthermore, the physical and electrochemical properties of as-sprayed or pre-heat-treated samples (TiO_2@NGC-AC MSB) and filled or non-porous samples (F-TiO_2/AC) were also obtained and compared.

2. Experimental

2.1. Materials synthesis

Three-dimensional TiO_2@NGC MSB, TiO_2@NGC-AC MSB, and F-TiO_2/AC samples were prepared using an easily scalable spray pyrolysis technique. A PS nanobead suspension (100 mL, $\phi = 100$ nm) was added to 100 mL of distilled water and stirred vigorously. The PS nanobeads used as pore generators were prepared using an emulsion polymerization technique, as reported previously [41]. Afterward, 0.15 M of titanium (IV) isopropoxide (TTIP; JUNSEI, $M_w = 284.23$) was added to the above solution, followed by the addition of an appropriate amount of nitric acid. Finally, 2.0 g of polyvinylpyrrolidone (PVP) (DAEJUNG, $M_w = 40{,}000$) was added as the carbon precursor. The resulting spray solution was stirred overnight under ambient conditions. Subsequently, the solution was transferred to an ultrasonic nebulizer connected to a vertical quartz reactor (Scheme S1). The droplets generated by the ultrasonic nebulizer were passed through a quartz reactor preheated at 600 °C in a N_2 atmosphere (10 L min^{-1}). The as-sprayed powders were further subjected to a heat treatment at 300 °C for 3 h at a ramp rate of 5 °C min^{-1} to form TiO_2@NGC MSB. In addition, the as-sprayed powder without heat treatment or TiO_2@NGC-AC MSB was employed as a comparison sample. Another comparison sample denoted as F-TiO_2/AC (F stands for "Filled") was also prepared without using PS nanobeads and PVP under identical preparation conditions.

2.2. Material characterization

The phase structures of the prepared TiO_2@NGC MSB, TiO_2@NGC-AC MSB, and F-TiO_2/AC powders were determined using a Bruker X-ray diffraction (D8) instrument employing Cu Kα radiation ($\lambda = 1.5418$ Å) at the Korea Basic Science Institute (Daegu). Microstructural characteristics were analyzed using field-emission scanning electron microscopy (FE-SEM) (UltraPlus; Zeiss) and field-emission transmission electron microscopy (FE-TEM) (JEM-2100F; JEOL). Thermogravimetric analysis (TGA) was used to quantify the carbon content from 25 to 600 °C at a ramp rate of 10 °C min^{-1} in an air atmosphere. The chemical states and bonding environments of the different elements in the as-prepared powders were determined using X-ray photoelectron spectroscopy (XPS) (K-Alpha; Thermo Scientific) with an Al Kα X-ray source. The specific surface area and pore size distribution of the as-prepared powders were determined using N_2 adsorption-desorption isotherms based on the Brunauer–Emmett–Teller (BET) method. Elemental analysis (EA) was employed to quantify the carbon and nitrogen content of the samples. The crystalline characteristics of the carbonaceous products in the prepared powders were studied using Raman spectroscopy (LabRam, HR800, Horiba Jobin-Yvon).

2.3. Cell assembly and electrochemical measurements

A typical slurry-casting method was employed to prepare anodes by mixing the as-prepared powders as the active material, super-P as a conductive agent, and sodium carboxymethyl cellulose as a binder in a mass ratio of 7:2:1 in a minimum amount of deionized water. This slurry was then coated onto a copper current collector and dried overnight in a hot-air oven preheated at 60 °C. The dried coated slurry was punched into circular electrodes ($\phi = 14$ mm) with an average active material loading of ~1.5 mg cm^{-2} and transferred to a glove box. The active material loading was fixed throughout the electrochemical characterization. CR2032 coin cells were assembled using the prepared electrodes as anodes, metallic Li as the anode, and microporous polypropylene film as a separator. The electrolyte used was 1.0 M $LiPF_6$ in a blend of fluoroethylene carbonate (FEC) and dimethyl carbonate (DMC) present in a volume ratio of 1:1. The rate capabilities of the assembled cells were measured at various current rates ranging from 0.2 to 10.0 A g^{-1} using a WBCS3000 (WonATech) battery cycle at 25 °C. The cycling performance

of the assembled cells was evaluated at 2.0 and 3.0 A g^{-1}. Cyclic voltammetry (CV) measurements were performed at a voltage scan rate of 0.1 mV s^{-1}. Electrochemical tests were conducted with the voltage range fixed at 0.001–3.0 V. Electrochemical impedance spectroscopy (EIS) data was collected to draw Nyquist plots in the frequency range of 100 kHz–0.01 Hz.

3. Results and discussion

3.1. Physical characterization results

The formation mechanism of the three-dimensional hierarchal porous NGC and anatase TiO_2 micro sponge-ball (TiO_2@NGC MSB) synthesized using the spray pyrolysis technique is presented in Scheme 1. During the first step, spray droplets were generated using an ultrasonic nebulizer comprising a homogeneously mixed colloidal solution of Ti-metal salt, PVP as a carbon source, and PS nanobeads ($\phi = 100$ nm) as a pore generator in distilled water, as shown in Scheme 1-①. The droplets were then dried by passing through the vertically aligned quartz reactor tube preheated at 600 °C (Scheme 1-②), resulting in the thermal breakdown of the metal salt to metal oxide; however, PVP decomposed into AC and NGC depending on the vicinity of the Ti species, which act as catalysts for the graphitization of C (Scheme 1-③). In addition, the PS nanobeads decomposed into gaseous products, generating numerous uniformly distributed macropores with a mean size of 80 nm inside and outside the prepared nanostructure. This resulted in the formation of a three-dimensional porous micro sponge-ball comprising anatase-TiO_2 nanodots and NGC-AC species (TiO_2@NGC-AC MSB) in the carbon matrix. During the second step, the as-sprayed TiO_2@NGC-AC MSB was subjected to heat treatment at 300 °C for selective removal of AC from the carbon matrix in the form of gaseous products, thus forming micropores in the nanostructure. This step resulted in a hierarchical porous three-dimensional micro sponge-ball consisting of a NGC framework and anatase-type titanium dioxide nanodots (TiO_2@NGC MSB), as shown in Schemes 1-④. The resulting micropores are believed to act as secondary sites for additional Li storage and, therefore, could be beneficial for enhancing the overall electrochemical performance [42].

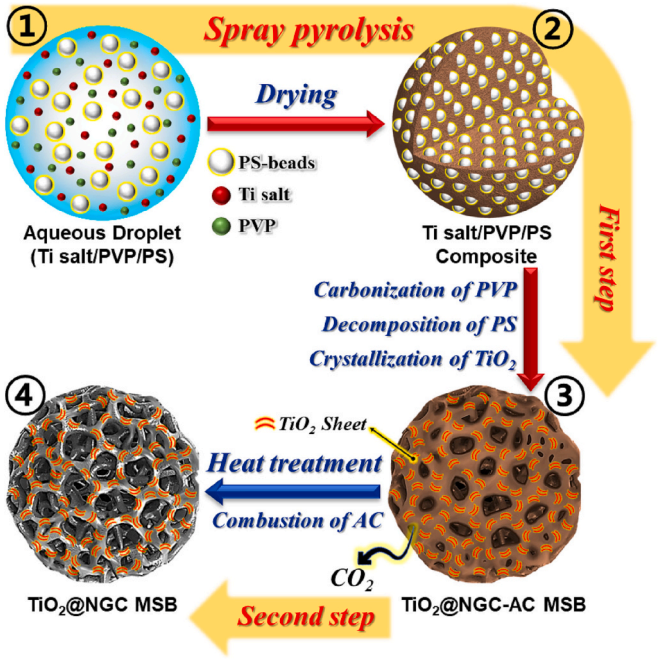

Scheme 1. Schematic representation (①-④) of the formation mechanism of three-dimensional hierarchically porous micro sponge ball comprising nitrogen-doped graphitic carbon-coated titanium dioxide nanodots (TiO_2@NGC MSB).

To elaborate the formation mechanism, a detailed microstructural analysis of the as-prepared three-dimensional hierarchically porous N-doped graphitic C and anatase TiO_2 micro sponge-balls (TiO_2@NGC MSB) was performed after each synthesis step. The morphological and crystal structure results of the sample obtained after spray pyrolysis at 600 °C in a N_2 atmosphere are shown in Fig. 1. The FE-SEM micrograph (Fig. 1a) of the as-sprayed sample indicated the formation of a non-aggregated 3D sponge-ball-like structure with an average diameter of 1.1 μm (Fig. S1a). The high-resolution FE-SEM image (Fig. 1b) suggested the presence of uniformly distributed macropores (mean pore diameter of 80 nm) inside and outside the micro sponge-ball. The formation of evenly distributed macropores can be ascribed to the decomposition of the PS nanobeads ($\phi = 100$ nm) at 600 °C during the spray pyrolysis. The shrinkage of the pore diameter from 100 to 80 nm after spray pyrolysis could be attributed to the contraction of the micro sponge-balls during the heat-treatment process. In addition, the micrographs revealed sparsely connected Ti species in the sponge-ball. It should be noted that the spray droplets passed through the vertical quartz tube in 4.8 s. During this short period, a fraction of the carbon source (PVP) was partially converted to AC and NGC, depending on the vicinity of the titanium species. Thus, the partially graphitized carbon matrix sparsely connect the titanium species to form a sponge-like nanostructure. Furthermore, the fractured surface image (Fig. 1c) of the 3D sponge-ball confirmed the presence of evenly distributed macropores in the internal structure. The TEM image in Fig. 1d confirmed the formation of a 3D sponge-ball with a diameter of 1.4 μm, which is consistent with the FE-SEM results. In addition, macro-sized open pores were also observed in the TEM image. The high-magnification TEM image (Fig. 1e) explicitly shows bright regions corresponding to the open pores (highlighted by arrows). Additionally, the dark region corresponds to the presence of TiO_2 nanodots embedded in the AC or NGC matrix. The high-resolution TEM (HR-TEM) image in Fig. 1f shows well-resolved lattice fringes for the (002) plane of the NGC layer (0.34 nm) and the anatase-type TiO_2 nanodots along with the AC. The average size of the TiO_2 nanodots was ca. 6 nm using HR-TEM images shown in Fig. S2a and b. The NGC layer primarily originates from the graphitization of the PVP surrounding the titanium species owing to their catalytic effect [43]. The NGC layer enhances the overall electrical conductivity of the micro sponge-ball owing to the higher electronegativity of nitrogen than that of carbon [38,39]. The lattice fringe spacing of 0.35 nm corresponded to the (101) plane of the anatase TiO_2 phase (Fig. 1g). The selected area electron diffraction (SAED) pattern in Fig. 1h displays well-defined diffraction rings corresponding to the anatase TiO_2 phase. Moreover, the diffraction ring corresponding to the NGC layer nearly superimposed the (101) plane of anatase TiO_2, owing to their similar lattice fringe spacing values. The XRD pattern in Fig. 1i confirmed the TEM results with all diffraction peaks indexed to the anatase TiO_2 crystal structure. The mean crystallite size of the anatase TiO_2 nanodot was determined to be 4.6 nm using the Scherrer equation corresponding to the highest intensity reflection plane, i.e., (101), and is consistent with the TEM/HR-TEM results discussed above. The elemental mapping results in the Fig. 1j indicate the uniform distribution of Ti, O, C, and N in the nanostructure, suggesting the formation of 3D micro sponge-balls comprising NGC/AC and anatase TiO_2 nanodots (TiO_2@NGC-AC MSB) and uniformly distributed PS nanobeads-derived macropores. The TiO_2@NGC-AC MSB powders were further subjected to heat treatment at 300 °C for 3 h to effectively control the crystalline structure and form micropores in the carbonaceous matrix. The FE-SEM micrographs in Fig. 2a implied that the 3D morphology of the powder remained intact even after heat treatment, with an average diameter of 1.1 μm (Fig. S1b). As evident from the high magnification FE-SEM image in Fig. 2b, the porous structure of the micro sponge-ball is more pronounced after heat treatment owing to the selective burning of AC to gaseous products. The fractured cross-sectional image in Fig. 2c also implied that a highly porous structure was well maintained inside the micro sponge-ball,

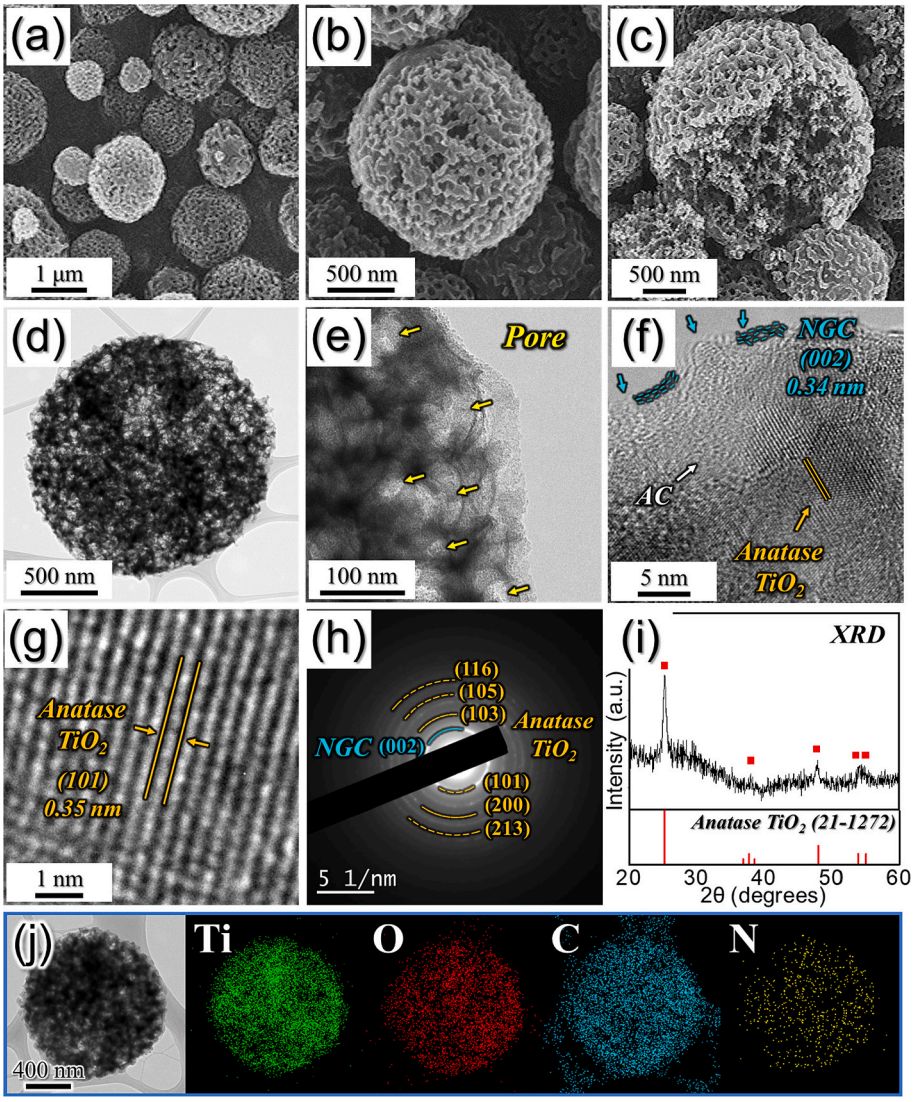

Fig. 1. Morphologies, SAED, XRD patterns and elemental mapping images of TiO_2@NGC-AC MSB obtained after spray pyrolysis at 600 °C: (a-c) FE-SEM images, (d, e) TEM images, (f, g) HR-TEM image, (h) SAED pattern, (i) XRD pattern, and (j) elemental mapping images.

despite a significant loss of AC species. This was further confirmed by the TGA and Raman spectra of the as-sprayed powders obtained before and after the heat treatment. The TG curve (Fig. S3a) for the TiO_2@NGC-AC MSB before heat treatment implied two major weight loss regions in an air atmosphere. The first region between 270 and 370 °C corresponded to the burning of AC to gaseous products ($\Delta m = -16$ %), whereas the second weight loss region from 370 to 500 °C ($\Delta m = -19$ %) can be assigned to the combustion of NGC species [44,45]. These results are consistent with the TG curve obtained for the as-sprayed powder after heat treatment (Fig. S3b), indicating a weight loss of 18 % between 390 and 490 °C owing to the burning of NGC species to gaseous products. The TGA results for the pre-heat-treated and heat-treated powders are well supported by the elemental analysis (EA) results in Table S1, which suggest a carbon content of ca. 32 wt% for the TiO_2@NGC-AC MSB powder compared to 14 % for the TiO_2@NGC MSB powder. The Raman spectrum was analyzed further to confirm the crystalline nature of the carbonaceous species before and after the heat treatment. The relative intensity ratio of the D and G bands (i.e., I_D/I_G) indicates the degree of crystallinity [46]. The Raman spectrum for TiO_2@NGC-AC MSB in Fig. S4a displayed an I_D/I_G value of 0.37, which indicates graphitic characteristics. However, it should be noted that TiO_2@NGC-AC MSB powder also contains AC (Fig. S3a). The oxidation process to obtain the TiO_2@NGC MSB effectively removes the AC thus resulting in the existence of NGC only, as evident by the TGA result (Fig. S3b). However, the slight increase in the I_D/I_G value (0.44; Fig. S4b) is due to the presence of defects in the graphitic carbonaceous species which formed during the oxidation process. Furthermore, the TEM images in Fig. 2d and e again confirm the 3D sponge-ball-like morphology of the prepared powders with evenly distributed macropores (bright regions) throughout the internal and external structures. The selective removal of AC also contributed to the total porosity of the sample owing to the formation of micropores (discussed in the BET section). The lattice fringe spacing of 0.34 nm (Fig. 2f) and 0.35 nm (Fig. 2g) is also evident, corresponding to the (002) and (101) planes of the NGC and anatase TiO_2, respectively. Moreover, the average size of TiO_2 nanodots in the TiO_2@NGC MSB was ca. 12 nm using the HR-TEM images presented in Fig. S2c and d. The SAED pattern in Fig. 2h shows well-resolved diffraction planes perfectly indexed to the anatase TiO_2 phase. The XRD pattern in Fig. 2i validates the phase purity of the prepared powders, which matches well with the anatase TiO_2 crystal structure. The mean crystallite size of the TiO_2 nanodot was determined to be 11.8 nm using the Scherrer equation from the highest intensity reflection plane, viz. (101). The elemental mapping images in Fig. 2j implied uniform distribution of Ti, O, C, and N. Overall, the above results confirmed the formation of a highly porous 3D micro

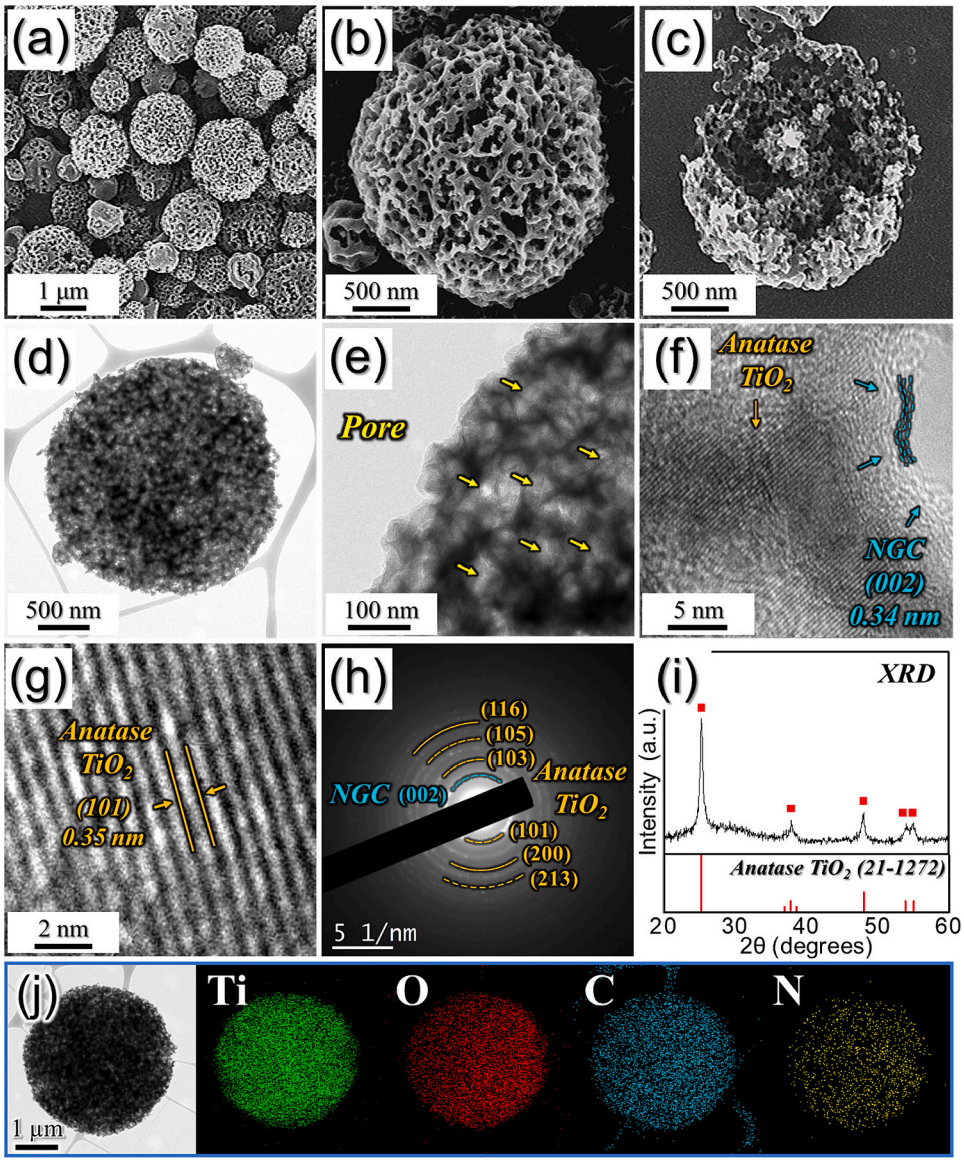

Fig. 2. Morphologies, SAED, XRD patterns and elemental mapping images of TiO_2@NGC MSB obtained after heat treatment at 300 °C: (a-c) FE-SEM images, (d, e) TEM images, (f, g) HR-TEM image, (h) SAED pattern, (i) XRD pattern, and (j) elemental mapping images.

sponge-ball comprising NGC and anatase TiO_2 nanodots with numerous macropores and micropores that eventually envisage improved electrochemical properties owing to the enhanced electronic conductivity, efficient electrolyte percolation, and presence of additional storage sites.

The bonding states and chemical environments of the different elements in the as-prepared TiO_2@NGC MSB were determined using XPS. The XPS survey spectrum in Fig. S5 shows photoelectron signals related to Ti 2p, O 1s, C 1s, and N 1s. The high-resolution Ti 2p XPS spectrum in Fig. 3a shows two well-fitted intense peaks at binding energies of 458.4 (Ti $2p_{3/2}$) and 464.1 (Ti $2p_{1/2}$) eV, which correspond to Ti^{4+} species in the prepared powders [43]. Moreover, a binding energy difference of ΔE = 5.7 eV between the two sharp peaks also confirms the strong interaction between Ti and O atoms [47]. Furthermore, two low-intensity signals located at 457.4 (Ti $2p_{1/2}$) and 460.9 eV (Ti $2p_{3/2}$) were fitted, corresponding to the Ti^{3+} cations in the Ti_2O_3 phase, which resulted from the incomplete oxidation of Ti species and matched well with previous reports [48]. However, the low intensity indicated a negligible proportion of the Ti_2O_3 phase in the as-prepared powders. The deconvoluted O 1s XPS spectrum in Fig. 3b exhibits well-resolved photoelectron peaks at 529.8, 531.8, and 533.2 eV that could be ascribed to the Ti—O, –OH, and C═O bonds, respectively [49,50]. The C 1s high-resolution XPS spectrum in Fig. 3c display three fitted peaks located at 284.4, 285.2, and 288.4 eV that could be attributed to the C═C, C–N/C–C, and C═O bonds, respectively [43,51–56]. The high-intensity peak corresponding to C═C indicates the presence of carbonaceous species in the as-prepared powders. Additionally, the peaks corresponding to C–N/C–C indicate N-doping of the carbonaceous skeleton [57–59]. N-doping mainly results in enhanced electronic conductivity owing to the higher electronegativity of the N atom compared to the C atom [39,60,61]. These results were confirmed by the deconvoluted N 1s XPS spectrum (Fig. 3d), which displayed four well-fitted distinct peaks centered at 398.6, 400.1, 401.6, and 403.6 eV corresponding to pyridinic, pyrrolic, graphitic, and oxidized N species, respectively [38,62,63]. These results confirm N-doping in the carbonaceous material framework in the form of NGC. Elemental analysis was performed to quantify the N content in the as-prepared powders (Table S1). The nitrogen content in the TiO_2@NGC MSB was estimated to be 1.8 wt%, mainly induced by the N-rich organic units present in the PVP polymer. However, the lower nitrogen content in the heat-treated sample compared to the pre-heat-treated sample (2.2 wt%) is due to the burning of a large proportion

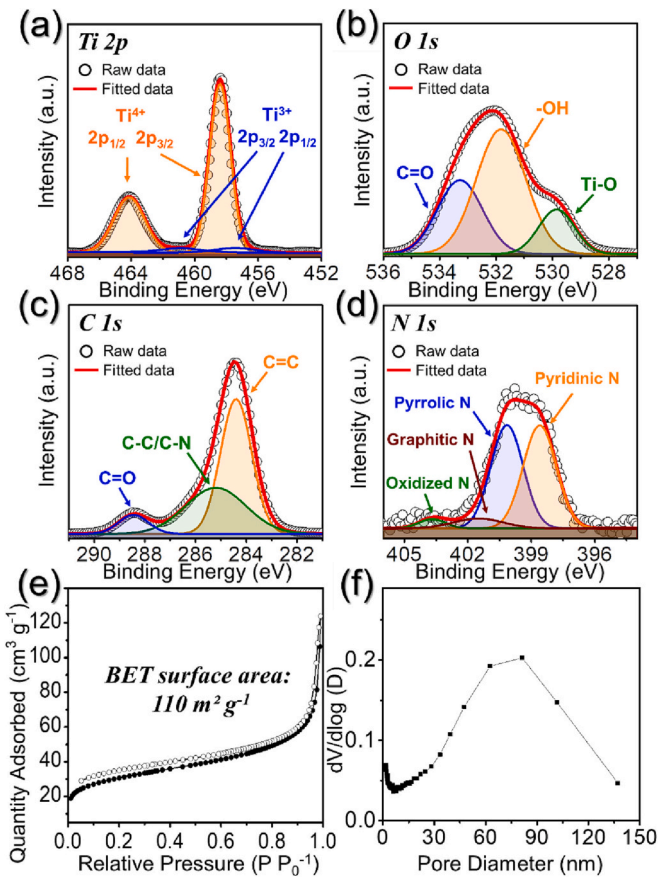

Fig. 3. XPS and BET characterization of TiO_2@NGC MSB: (a) core-level Ti 2p XPS spectra, (b) core-level O 1s XPS spectra, (c) core-level C 1s XPS spectra, (d) core-level N 1s XPS spectra, (e) N_2 adsorption-desorption isotherms, and (f) BJH desorption pore-size distributions.

of N-doped carbonaceous species during the heat treatment, as predicted from the TG curve (Fig. S3b). The BET surface area of the as-prepared powders was determined using N_2 adsorption–desorption isotherms and was observed to be 110 $m^2\ g^{-1}$ for the TiO_2@NGC MSB (Fig. 3e), which is much higher than that of the TiO_2@NGC-AC MSB powder (25 $m^2\ g^{-1}$) before heat treatment (Fig. S6a). The high BET surface area of the TiO_2@NGC MSB is primarily owing to the newly formed micropores in the nanostructure during the heat treatment, as evident from the micropore distribution curve in Fig. S7. Therefore, the BET results suggested that the synergistic effects of the PS nanobeads-derived macropores and AC-combustion-induced micropores significantly enhance the porosity of the nanostructure, which eventually facilitates the rapid transportation of charged species and efficient electrolyte penetration. In addition, the micropores thus formed offer additional secondary sites for more Li storage and are therefore helpful in improving the overall electrochemical performance [42]. The Barrett–Joyner–Halenda pore size distribution curve shown in Fig. 3f suggested the presence of macropores with a peak maximum centered at ~82 nm, along with an increased micropore density. Similarly, the pore size curve (Fig. S6b) for the TiO_2@NGC-AC MSB powder before heat treatment implied the presence of macropores (~91 nm) produced only by PS decomposition.

For better comparison, filled-structured anatase TiO_2/AC composite powders were also prepared from the spray suspension with Ti salt and without both PVP and PS nanobeads under identical spray conditions. Morphological and crystal structure analyses of the as-sprayed samples are presented in Fig. S8. The FE-SEM micrograph in Fig. S8a indicated the formation of non-aggregated 3D spherical balls with a mean diameter of ~ca. 600 nm. In addition, the smooth surface observed in Fig. S8b indicated the absence of pores in the prepared powder. Furthermore, the fractured FE-SEM micrograph (inset in Fig. S8b) and the TEM micrograph (Fig. S8c) confirmed the filled structure. Thus, the as-sprayed powder was denoted as "F-TiO_2/AC" where F stands for "Filled" or non-porous. The HR-TEM image in Fig. S8d shows a clear lattice fringe spacing of 0.35 nm corresponding to the (101) diffraction plane of the anatase TiO_2 crystal structure. The SAED pattern in Fig. S8e indicates well-fitted diffraction rings corresponding to the various crystal planes of anatase TiO_2. The phase purity of the as-sprayed powder was determined by XRD spectrum (Fig. S8f), indicating an anatase TiO_2 crystal structure with an average crystallite size of 8.04 nm. The elemental dot mapping results (Fig. S8g) confirmed the presence of Ti, O, and C in the as-sprayed powder. Moreover, a small amount of AC (~3.8 wt%) was confirmed by the TGA curve (Fig. S9). AC primarily originates from the tetra isopropoxide ($C_{12}H_{28}O_4$) units in the titanium salt (TTIP ➔ TiO_2 + $4C_3H_7OH$). The non-porosity of the F-TiO_2/AC powder was confirmed by obtaining the BET surface area (Fig. S10a), which suggested a low value of 14 $m^2\ g^{-1}$ owing to the absence of pores, as indicated by the pore size curve in Fig. S10b.

3.2. Electrochemical performance

To prove the structural superiority of the TiO_2@NGC MSB, TiO_2@NGC-AC MSB, and F-TiO_2/AC powders, their electrochemical performances were analyzed using a CR2032 coin cell. The CV results of the TiO_2@NGC MSB for the first five cycles at a scan rate of 0.1 mV s^{-1} in the voltage range of 0.001–3.0 V are shown in Fig. 4a. The shape of the CV curve suggested that the redox reactions inside the cell are mainly governed by two processes: the faradaic-type Li-ion insertion-extraction and the non-faradaic-type capacitive process. During the initial discharge, the insertion of Li-ions resulted in an irreversible transformation of anatase TiO_2 to lithium titanate at 1.0 V vs. Li^+/Li, mainly owing to the formation of a SEI and irreversible electrochemical reactions, such as the reduction of $Ti^{4+} \rightarrow Ti^{3+}$ [23,64]. In addition, the sharp peak at 0.001 V implied the insertion of Li-ions into the carbonaceous species [31]. The high intensity of the first reduction process for the TiO_2@NGC MSB compared with that of the TiO_2@NGC-AC MSB (Fig. S11a) and F-TiO_2/AC (Fig. S11b) powders implied that more interstitial octahedral sites are available for the reduction process between Li-ions and anatase TiO_2 because of its high surface area. Similarly, the oxidation peak at 0.18 V during the first anodic scan indicated the extraction of Li-ion from the carbonaceous material, whereas the noticeable hump at 2.05 V signified the oxidation of lithium titanate back to the anatase TiO_2 phase [64]. More symmetric CV curves were obtained during the second CV scan, with cathodic-anodic peak pairs centered at 1.73/2.05 and 0.001/0.15 V, indicating reversible Li-ion movement into the anatase TiO_2 crystal structure ($xLi^+ + TiO_2 + xe^- \leftrightarrow Li_xTiO_2$; $x = 0.5$) and carbon matrix, respectively. The CV curves began to overlap significantly with their shapes intact after the second cycle onwards, suggesting highly reversible electrochemical redox reactions inside the cell. TiO_2@NGC-AC MSB powder also displayed similar CV characteristics (Fig. S11a), despite its lower current intensity than that of the TiO_2@NGC MSB sample, indicating relatively sluggish redox processes inside the cell. Similarly, the F-TiO_2/AC (Fig. S11b) also displayed analogous CV characteristics with minor differences. For instance, the existence of a shoulder peak at 1.74 V during oxidation is mainly because of the presence of a few interstitial defects in the F-TiO_2/AC crystal structure [65]. The initial charge-discharge voltage profiles were analyzed for all the prepared powders to verify the CV results at a current density of 1.0 A g^{-1}, as shown in Fig. 4b. The obtained voltage profiles were in good agreement with the CV results, with no obvious charge and discharge voltage plateaus. The initial charge/discharge capacities of TiO_2@NGC MSB, TiO_2@NGC-AC MSB, and F-TiO_2/AC powders were determined to be 240/589, 145/372, and 51/114 mA h g^{-1}, respectively. Additionally, the initial Coulombic efficiencies (ICEs) of the TiO_2@NGC MSB, TiO_2@NGC-AC MSB, and F-TiO_2/AC powders

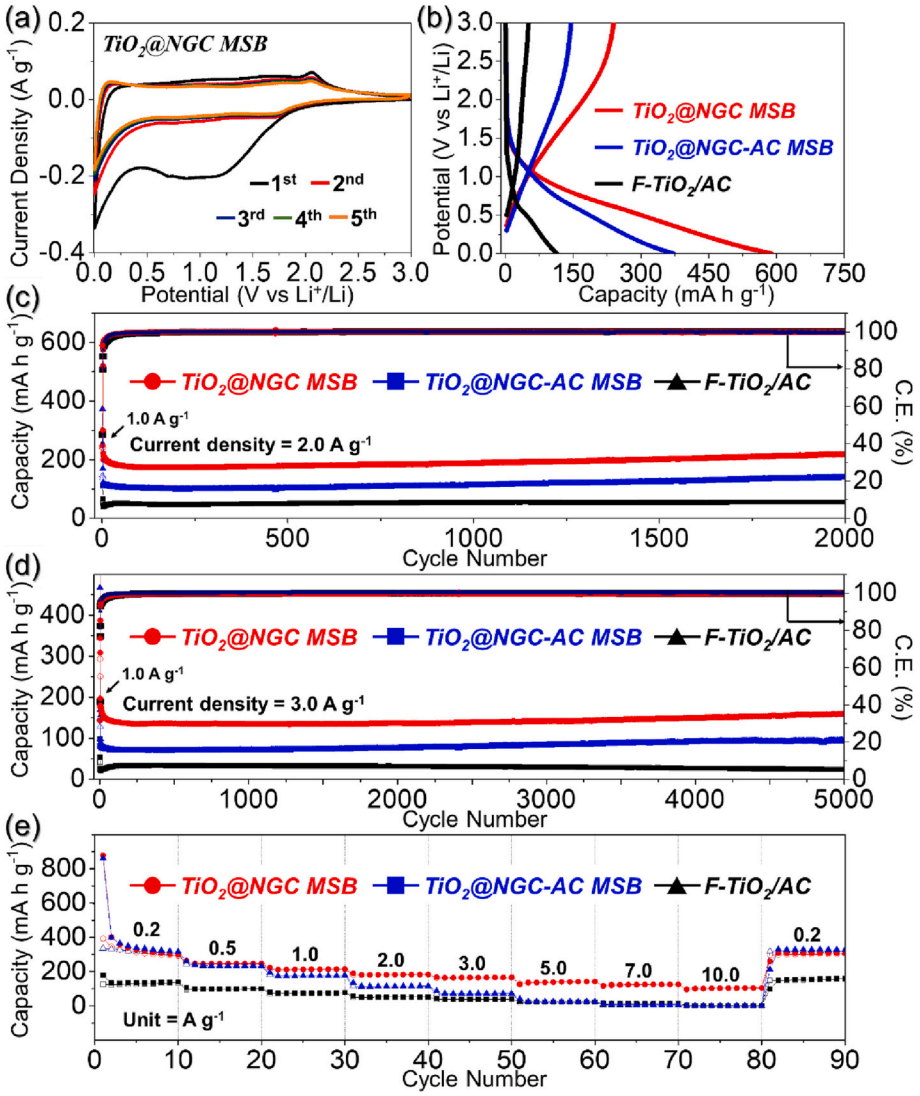

Fig. 4. Electrochemical properties of TiO_2@NGC MSB, TiO_2@NGC-AC MSB, and F-TiO_2/AC for Li-ion storage: (a) CV curve of TiO_2@NGC MSB, (b) initial discharge/charge curves at a constant current density of 1.0 A g^{-1}, (c) cycle performance at current density of 2.0 A g^{-1}, (d) cycle performance at current density of 3.0 A g^{-1}, and (e) rate performances.

were 41, 45, and 40 %, respectively. Moreover, the cell utilizing the TiO_2@NGC MSB anode displayed the lowest polarization potential ($\Delta V = 0.70$ V) compared with those of the TiO_2@NGC-AC MSB ($\Delta V = 0.88$ V) and F-TiO_2/AC ($\Delta V = 1.35$ V) powders. The high initial discharge capacity, reasonable ICE, and lowest polarization potential of the TiO_2@NGC MSB suggested that the hierarchical porous structure not only guarantees superior electrolyte percolation owing to evenly distributed macropores but also ensures improved electronic/ionic conductivities because of NGC, in addition to facilitating rapid charge diffusion processes that result in enhanced redox kinetics. Overall, the CV and initial charge/discharge voltage profiles confirmed the structural dominance of the TiO_2@NGC MSB powder compared to the TiO_2@NGC-AC MSB and F-TiO_2/AC powders.

The cycling performances of the as-prepared powders were also evaluated at current densities of 2.0 and 3.0 A g^{-1}, as shown in Fig. 4c and d, respectively. The cell utilizing the hierarchically porous TiO_2@NGC MSB anode exhibited superior and stable cycling performance at each current density compared with the TiO_2@NGC-AC MSB and F-TiO_2/AC anodes. For instance, the TiO_2@NGC MSB anode displayed a discharge capacity of 222 mA h g^{-1} at a current density of 2.0 A g^{-1} (Fig. 4c), which almost remained constant during cycling and stabilized at 219 mA h g^{-1} at the end of the 2000th cycle. This suggested capacity retention of 99 % with an ultra-low average capacity decay rate of just 0.0006 % per cycle. By contrast, the cells employing the TiO_2@NGC-AC MSB and F-TiO_2/AC anodes exhibited discharge capacities of 122 and 44 mA h g^{-1}, respectively, which increased to 139 (82 % retention) and 56 (85 % retention) mA h g^{-1} after 2000 cycles. Besides, the average capacity decay rates of 0.008 and 0.007 % per cycle were observed for the TiO_2@NGC-AC MSB and F-TiO_2/AC anodes, respectively. Additionally, CE values over 99.8 % for the TiO_2@NGC MSB indicated highly reversible electrochemical performance inside the assembled cells. Similar results were obtained when cycling was performed at a higher current density of 3.0 A g^{-1} (Fig. 4d). The cells utilizing the TiO_2@NGC MSB, TiO_2@NGC-AC MSB, and F-TiO_2/AC anodes exhibited discharge capacities of 198, 99, and 26 mA h g^{-1}, respectively. At the end of the 5000th cycle, the discharge capacity of the TiO_2@NGC MSB anode stabilized at 160 mA h g^{-1} compared to the 94 and 24 mA h g^{-1} for the TiO_2@NGC-AC MSB and F-TiO_2/AC anodes, respectively, at the end of identical cycle number. In addition, the anodes maintained a high CE throughout prolonged cycling, implying highly reversible and kinetically favored redox reactions inside the cell. However, the high and ultra-stable discharge capacity of the TiO_2@NGC MSB can be attributed to the highly porous structure that accommodates the volume expansion of anatase TiO_2 nanodots during Li-ion insertion and

extraction. This eventually stabilized the nanodot morphology and hence alleviated pulverization in the electrode architecture during the extended repeated cycling in an intentionally selected wide operating voltage range (0.001–3.0 V). Additionally, the electrochemical properties of NGC matrix (i.e., without TiO_2 nanodots) were also investigated to calculate the capacity contribution of the NGC matrix to the total capacity of TiO_2@NGC MSB. For the same, the TiO_2@NGC MSB powder was treated for 3 days with blended solution of hydrofluoric acid (45 %), hydrogen peroxide (35 %), and distilled water in a volume ratio of 1:1:20, respectively, to remove the Ti species followed by repeated washing with distilled water and subsequent drying at 100 °C in an air oven for overnight. The obtained electrochemical results are summarized in Fig. S12. The CV curves obtained at 0.1 mV s^{-1} (Fig. S12a) clearly indicate the redox processes for carbon only, with three peaks at 0.73/0.33 V and 0.001 V corresponding to the formation of SEI layer and lithium intercalation, respectively, in the NGC matrix [52,66]. The initial charge/discharge profiles of NGC matrix (Fig. S12b) at a current density of 1.0 A g^{-1} further supported these results. The cycle performance obtained at a current density of 2.0 A g^{-1} (Fig. S12c) indicated that the NGC matrix had a discharge capacity of 159 mA h g^{-1} at the 100th cycle. Correspondingly, the capacity contribution of the NGC matrix in the total capacity of TiO_2@NGC MSB was approximately 13 % (considering the carbon content of 14 wt%). Similarly, the NGC matrix had a discharge capacity of 114 mA h g^{-1} at the 100th cycle (at 3.0 A g^{-1}; Fig. S12d) thus indicating a capacity contribution of ca. 9 %. Therefore, the above results confirm that NGC matrix only acts as a conductive scaffold for the rapid charge transfer during the electrochemical process.

Rate capability tests were also conducted at current densities ranging from 0.2 to 10.0 A g^{-1} for the as-prepared anodes to further verify their structural merits (Fig. 4e). The hierarchical porous TiO_2@NGC MSB anode exhibited discharge capacities of 300, 248, 215, 184, 167, 143, 126, and 105 mA h g^{-1} for the 10th cycle at current densities of 0.2, 0.5, 1.0, 2.0, 3.0, 5.0, 7.0, and 10.0 A g^{-1}, respectively. The obtained capacities are superior to those of the TiO_2@NGC-AC MSB and F-TiO_2/AC anodes, which exhibited discharge capacities of 318/139, 234/102, 179/77, 117/53, 73/40, 25/23, 7/12, and 1/2 mA h g^{-1}, respectively, at identical current densities. When the current was reversed to 0.2 A g^{-1}, a comparable discharge capacity was obtained for the TiO_2@NGC MSB anode. The high discharge capacity of the TiO_2@NGC MSB anode, particularly at high current densities, confirms its structural superiority over TiO_2@NGC-AC MSB and F-TiO_2/AC anodes. The evenly distributed macropores not only facilitate efficient electrolyte percolation into the electrode during repeated cycling but also alleviate electrode pulverization by accommodating volume variations. Similarly, the presence of micropores offers additional sites for lithium insertion and extraction, thus increasing the overall capacity [42]. Besides, the NGC coating enhanced the overall electrical conductivity of the electrode, thus facilitating rapid charge transfer during redox reactions. The electrochemical performance of the present TiO_2@NGC MSB anode is summarized and thoroughly compared with other anatase TiO_2/C-based composite anodes in Table S2, which implied superior electrochemical properties for the proposed anode.

CV curves were obtained to get a better insight into the reaction kinetics inside the assembled cells of the as-prepared powders in the voltage range of 0.001–3.0 V at different scan rates (Fig. 5a). New peak pairs (denoted as R2/O2 and O3) were observed in the CV curves in addition to the original redox peak pairs (R1/O1), particularly at high-voltage scan rates. The R2/O2 redox peak pair could be attributed to the movement of Li-ions into the Ti^{3+} species (i.e., Ti_2O_3), whereas the O3 peak is ascribed to the emergence of new electrochemical sites originating from interstitial defects in the TiO_2 crystal structure, as reported previously [65]. Additionally, the CV curve shape indicates that different electrochemical processes occur simultaneously, such as faradaic-type Li-ion diffusion-controlled redox reactions, faradaic-type charge-transfer processes at the electrode surface (pseudocapacitance), and non-faradaic-type double-layer capacitive processes. To differentiate between the diffusion- and surface-controlled reactions, the peak current (i) values obtained during the electrochemical reactions were plotted against the voltage sweep rates (v) governed by the following power-law equation [67]:

$$i = av^b \tag{1}$$

$$log(i) = blog(v) + log(a) \tag{2}$$

Here, the extent of diffusion-controlled and capacitive-controlled processes is determined by variables a and b. For instance, if b approaches 1.0, the redox process is mainly capacitive or surface-controlled, whereas if b tends to 0.5, it is mainly diffusion-controlled, similar to battery processes [64]. The b values were determined using the slope of the log(i) versus log(v) plot, as shown in Fig. 5b. As observed, the b-values for the various redox peaks of the TiO_2@NGC MSB were close to 1, implying a surface-dominant or capacitive-controlled electrochemical process. By contrast, the reaction dynamics for the TiO_2@NGC-AC MSB anode depicted in Fig. S13a and b exhibit relatively lower b values, indicating that the redox processes are still capacitive-controlled but to a lesser extent. The reaction kinetics for the F-TiO_2/AC anode depicted in Fig. S13c and d indicate the lowest b values, suggesting the highest proportion of diffusion-controlled processes among all prepared samples. To quantify the contribution of capacitive and diffusion-controlled processes, each process was separated from the area under the total charge storage curve using the following equation [68,69]:

$$i = k_1v + k_2v^{1/2} \tag{3}$$

where k_1v and $k_2v^{1/2}$ represent the capacitive-controlled and diffusion-controlled contributions, respectively, and k_1 and k_2 are constants obtained from the slope and intercept of the $i(V)/v^{1/2}$ vs. $v^{1/2}$ plot, respectively. Fig. 5c shows a capacitive contribution factor (k_1v) of 81 % at a scan rate of 2.0 mV s^{-1} for the TiO_2@NGC MSB anode, as highlighted by the red area. Even at scan rates other than 2.0 mV s^{-1}, the TiO_2@NGC MSB anode exhibited capacitive-dominant reaction dynamics, as shown in Fig. 5d. Likewise, the surface-controlled reaction contributions for the TiO_2@NGC-AC MSB (Fig. 5e and f) and F-TiO_2/AC anode (Fig. 5g and h) also suggested a capacitive-dominant process, but at a lower percentage. These results confirmed the structural advantages of the TiO_2@NGC MSB anode, which facilitates not only kinetically favored rapid Li-ion transport and efficient electrolyte infiltration owing to the hierarchical porous nanostructure but also guarantees rapid charge transfer owing to the highly conducting NGC network.

The superior Li-ion transport properties of the TiO_2@NGC MSB anode were validated further using electrochemical impedance spectroscopy (EIS) (Fig. 6). Nyquist plots for fresh and cycled cells at different cycling numbers were recorded in a fully charged state. In addition, the EIS data were fitted using the deconvoluted Randle-type equivalent circuit model, as shown in Fig. S14, and the fitted parameter values are summarized in Table S3. The Nyquist plots for the fresh cells (Fig. 6a) exhibit similar solution resistance (R_s) values (~17 Ω), indicating identical interfacial redox processes at the electrode–electrolyte intersection. Furthermore, the charge transfer resistance (R_{ct}) values for the TiO_2@NGC MSB, TiO_2@NGC-AC MSB, and F-TiO_2/AC were 268, 234, and 190 Ω, respectively. However, after the 1st cycle, a significant decrease in R_{ct} was observed for all the samples, as shown in Fig. 6b. At the end of the 300th cycle (Fig. 6c), the R_{ct} values for the TiO_2@NGC MSB, TiO_2@NGC-AC MSB, and F-TiO_2/AC anodes were 27, 37, and 13 Ω, respectively. The lowest R_{ct} value for F-TiO_2/AC can be attributed to the non-porous nature of the sample, which resulted in a low contact surface area. However, the higher R_{ct} values for the TiO_2@NGC MSB and TiO_2@NGC-AC MSB anodes could be attributed to the presence of porous structures and conductive or nonconductive carbon skeletons. For instance, the presence of a porous structure in both

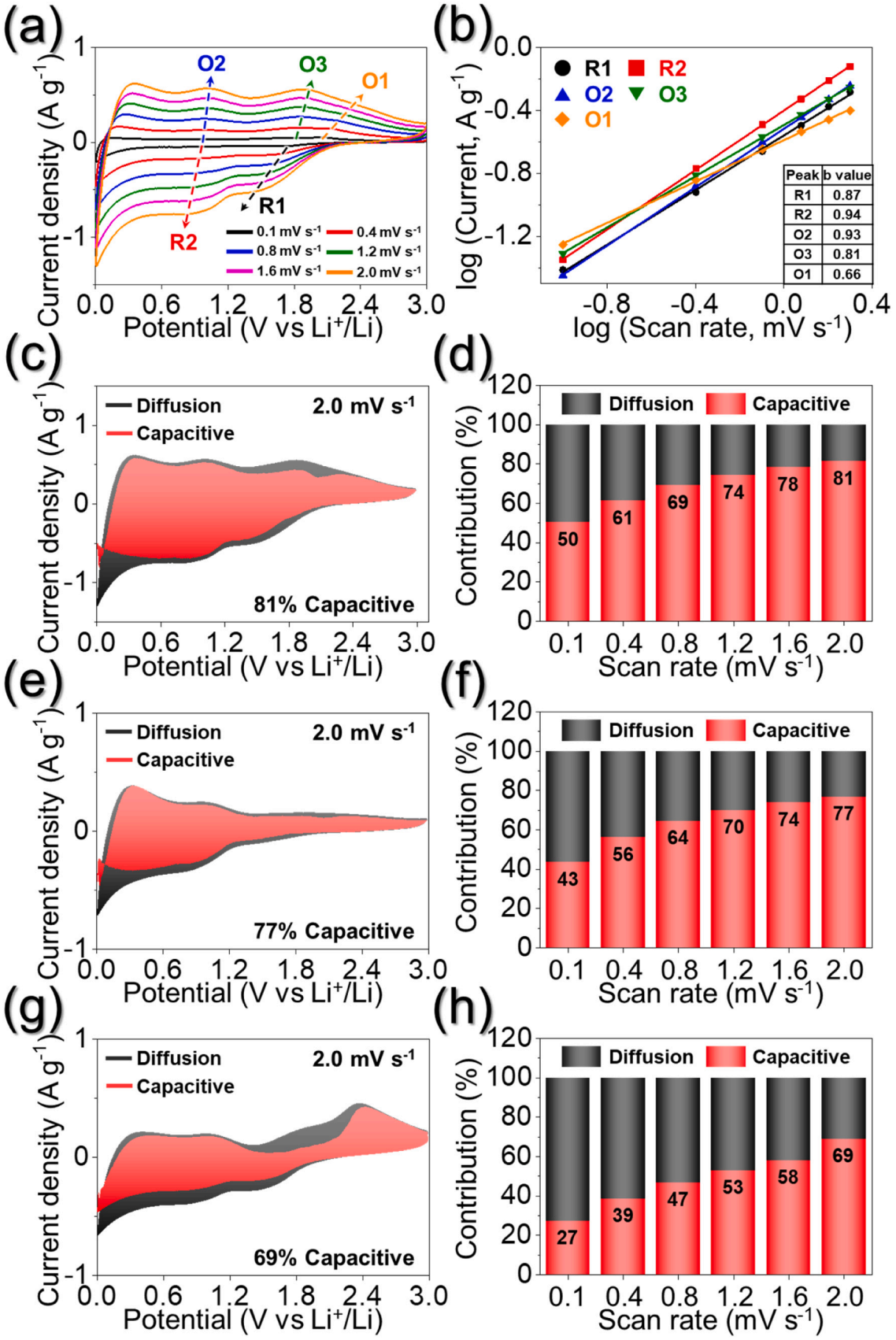

Fig. 5. Electrochemical reaction dynamics analysis of (a-d) the TiO_2@NGC MSB, (e, f) TiO_2@NGC-AC MSB, and (g, h) F-TiO_2/AC for Li-ion storage: (a) CV curves obtained at various scan rates, (b) current response (*i*) vs. scan rate (*n*) at each redox peak, (c, e, g) CV curves with the capacitive fraction shown by the red region at a scan rate of 2.0 mV s^{-1}, and (d, f, h) bar chart showing the percentage of the capacitive contribution at different scan rates. (For interpretation of the references to colour in this figure legend, the reader is referred to the web version of this article.)

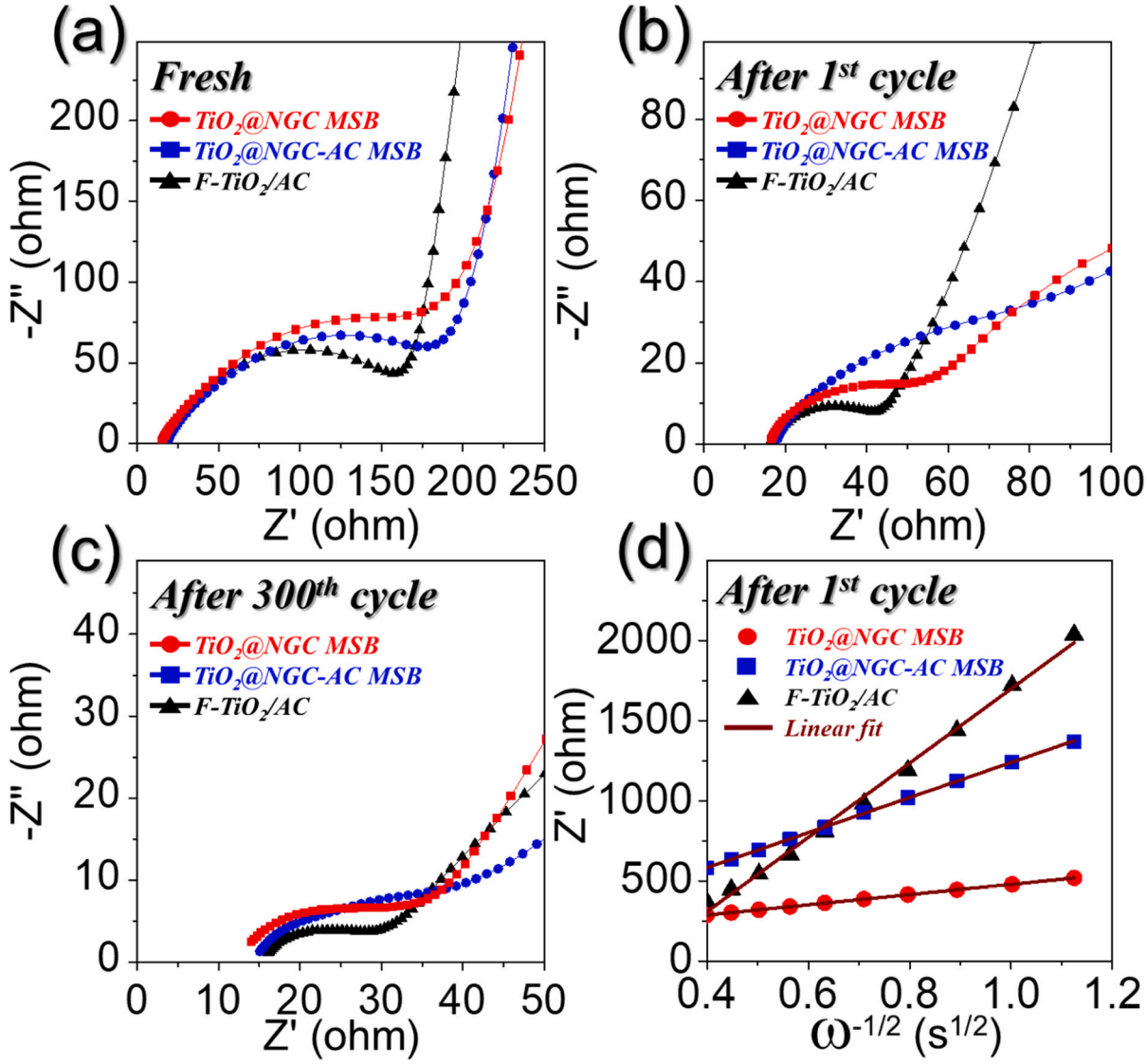

Fig. 6. Nyquist impedance plots of the TiO_2@NGC MSB, TiO_2@NGC-AC MSB, and F-TiO_2/AC: (a) before cycling, (b) after 1st cycle, (c) after 300th cycle, and (d) relationship plot between real part of the impedance (Z').

samples resulted in large contact surface areas and, therefore, a high R_{ct}. However, the low R_{ct} for the TiO_2@NGC MSB is because of the presence of the NGC framework, which facilitates fast electron transfer. By contrast, the presence of AC alongside NGC in the TiO_2@NGC-AC MSB retards electron movement during the redox processes, resulting in a higher charge transport resistance. Furthermore, the real part of the impedance Z' was plotted against $\omega^{-1/2}$ ($\omega = 2\pi f$ is the angular frequency) in the low-frequency region after the 1st cycle for all samples, as shown in Fig. 6d. The gentle slope for the cell employing the TiO_2@NGC MSB anode indicates higher Li-ion diffusion during the electrochemical reactions than the TiO_2@NGC-AC MSB and F-TiO_2/AC anodes. The Li-ion diffusion coefficient (D_{Li^+}) values were further quantified using Z' vs. $\omega^{-1/2}$ plots by employing the following equation [70–72]:

$$D_{Li^+} = \frac{0.5R^2T^2}{A^2F^4C^2\sigma_W^2} \quad (4)$$

where D_{Li^+} denotes the Li-ion diffusion coefficient, R represents the gas constant, T is the temperature, A stands for electrode area, C is the Li-ion concentration, F represents the Faraday constant, and σ_W is the Warburg impedance factor. The cell utilizing the TiO_2@NGC MSB anode exhibited a diffusion coefficient value one order of magnitude higher (1.37×10^{-13} cm^2 s^{-1}) than that of the TiO_2@NGC-AC MSB (1.71×10^{-14} cm^2 s^{-1}) and two orders of magnitude higher than that of F-TiO_2/AC (2.61×10^{-15} cm^2 s^{-1}). Therefore, the high D_{Li^+} values for the TiO_2@NGC MSB anodes indicated that the synergistic effects of the porous and conductive structures guarantee rapid charge diffusion during repeated cycling and enhance electrode integrity.

3.3. Post-cycling characterization results

To investigate the electrochemical performance of the TiO_2@NGC MSB after the cycling process, particularly the cycling performance, post-cycling characterizations of the TiO_2@NGC MSB anode are presented in Fig. 7. The cycled electrodes were carefully removed from the cells inside the glove box and dried. The high-magnification TEM image in Fig. 7a indicates that the spherical morphology of the TiO_2@NGC MSB remained intact even after 2000 cycles at 3.0 A g^{-1}, which suggested the high structural integrity of the prepared anode. The HR-TEM image in Fig. 7b shows clear lattice fringes corresponding to the (101) diffraction plane. Moreover, the lattice fringe spacing increased from 0.35 to 0.39 nm for the cycled TiO_2@NGC MSB, which suggested that the repeated Li-ion insertion and extraction resulted in the expansion of the crystal structure along the *c*-axis. This expansion is believed to

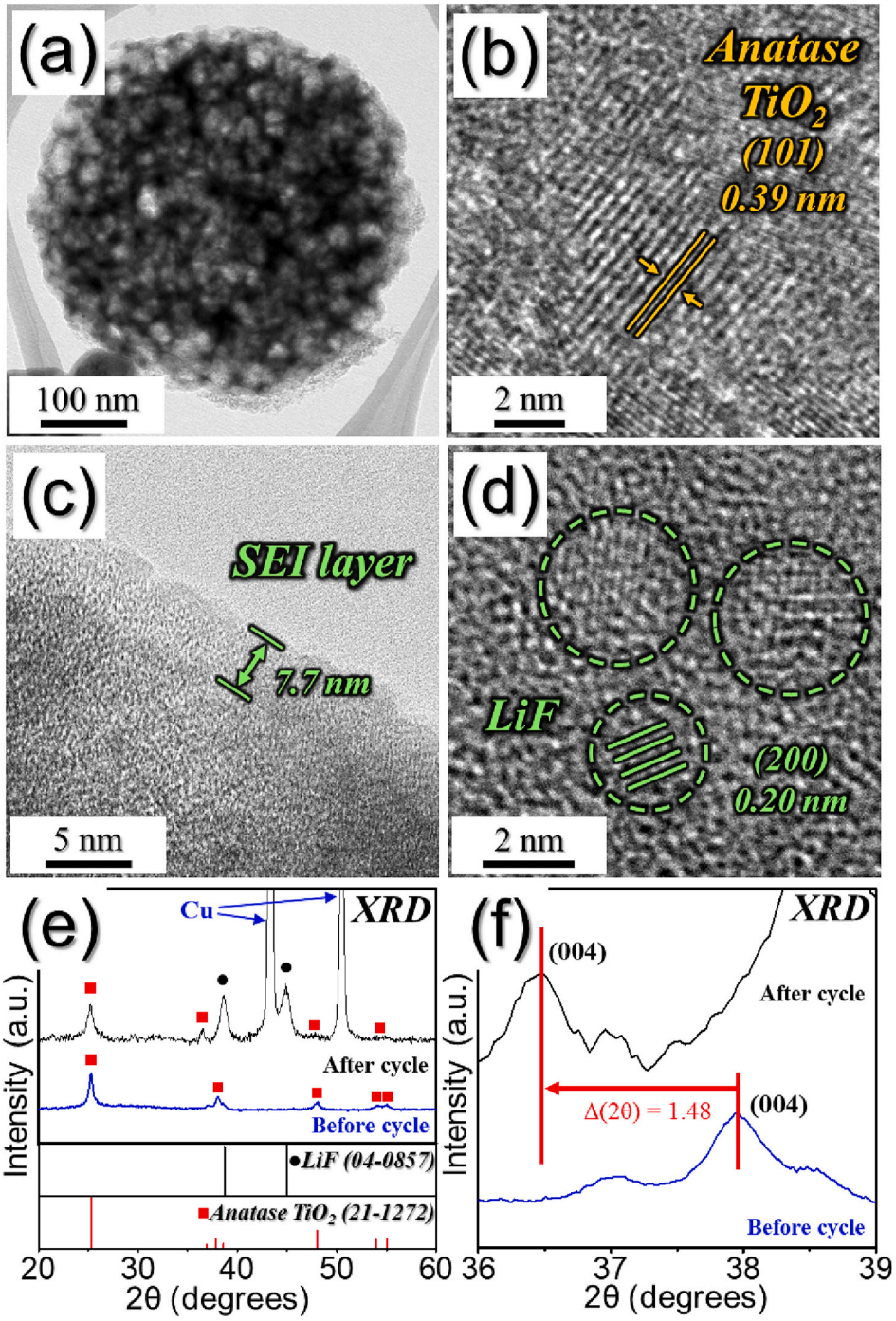

Fig. 7. Morphologies and XRD patterns of TiO_2@NGC MSB obtained after 2000 cycles at current density of 3.0 A g^{-1}: (a) TEM images, (b-d) HR-TEM images, and (e, f) XRD patterns.

induce structural defects in the crystal structure, which facilitates more insertion and/or extraction of Li-ions during repeated redox processes. Furthermore, the HR-TEM image in Fig. 7c indicates the presence of SEI layer (7.7 nm thick) formed due to the electrolyte decomposition in an intentionally chosen wide operating voltage range (0.001–3.0 V). Moreover, the SEI layer remained highly stable and continuous even after prolonged cycling, which could be attributed primarily to the structural robustness and integrity of the as-prepared hierarchically porous spherical sponge-ball. The HR-TEM image in Fig. 7d implies a clear lattice fringe spacing of 0.20 nm that corresponds to the (200) diffraction plane of the LiF derivative of electrolyte decomposition. We believe that synergistic effect occurs between the structural defects induced by the anatase TiO_2 crystal expansion and the SEI layer, which facilitates the simultaneous insertion and extraction of more Li-ions and their rapid transport at the electrolyte–electrode interface, resulting in excellent cycling performance. Furthermore, the broad-range XRD pattern and its magnified image also support the TEM results. For instance, a significant difference between the peaks of the cycled electrode and uncycled powder was observed in the XRD pattern (Fig. 7e). The XRD peaks for the cycled electrode correspond to the anatase phase of TiO_2, Cu current collector, and LiF species. Additionally, a clear shift of the (004) peak in Fig. 7f for anatase TiO_2 phase to lower 2θ is also in good accordance with the HR-TEM results in Fig. 7b, confirming the lattice expansion during prolonged cycling. Overall, the exceptional

cycling performance of the TiO_2@NGC MSB anode could be attributed to its high structural integrity or robustness, stable SEI layer, and expanded crystal structure that collectively allows faster and repeated insertion and/or extraction of Li-ions.

4. Conclusions

In this study, a design strategy was proposed to develop a hierarchically porous three-dimensional micro sponge-ball comprising nitrogen-doped graphitic carbon and the anatase titanium dioxide nanodots (TiO_2@NGC MSB) via an easily scalable spray pyrolysis method followed by a heat-treatment process. The as-sprayed nanostructure comprised of PS nanobead-derived macropores and anatase TiO_2 nanodots well embedded inside the carbonaceous matrix made up of NGC and AC. The heat-treatment step at 300 °C selectively removed AC to form the gaseous products. Consequently, an extremely porous micro sponge-ball comprising anatase-type TiO_2 nanodots and highly conductive NGC was obtained. The presence of PS and AC-derived porous structures offers efficient electrolyte penetration into the electrode, along with the rapid diffusion of charged species. The NGC composite enhanced the overall electrical conductivity and allowed fast reaction kinetics via smooth electron transfer. Highly stable anatase TiO_2 provides numerous electrochemically active sites. Consequently, the obtained TiO_2@NGC MSB nanostructure displayed overall improved electrochemical performance, such as high-rate capability and extremely stable cycling properties, compared to the TiO_2@NGC-AC MSB and F-TiO_2/AC anodes. The simplicity of the preparation method provides excellent possibilities for scaling it up to the commercial level to assemble half or full cells for various rechargeable energy storage systems.

Declaration of competing interest

The authors declare no competing financial interest.

Data availability

No data was used for the research described in the article.

Acknowledgments

This work was supported by the National Research Foundation of Korea (NRF) grant funded by the Korean government (MSIP) [No. NRF-2021R1A4A2001687, and NRF-2021R1I1A3057700]. This work was partly supported by Korea Institute of Energy Technology Evaluation and Planning (KETEP) grant funded by the Korea government (MOTIE) [20224000000070, Human Resource Training for Smart Energy New Industry Cluster].

CRediT authorship contribution statement

Jae Seob Lee and Hye Seon Ka: Conceptualization, Methodology, and Data curation. **Rakesh Saroha:** Visualization, Preparation of original draft. **Yun Chan Kang and Dong-Won Kang:** Research guidance. **Jung Sang Cho:** Writing-Reviewing-Editing and Supervision.

Appendix A. Supplementary data

Supplementary data to this article can be found online at https://doi.org/10.1016/j.est.2023.107396.

References

[1] Q. Zhang, X. Li, Recent developments in the doped-Li4Ti5O12 anode materials of lithium-ion batteries for improving the rate capability, Int. J. Electrochem. Sci. 8 (2013) 6449–6456.
[2] R. Saroha, A.K. Panwar, A. Jain, J. Singh, S. Verma, Development and electrochemical performances of Li3V2(PO4)3 and Li4Ti5O12 materials for lithium-ion battery, Ionics 23 (2017) 2631–2639, https://doi.org/10.1007/s11581-017-1984-2.
[3] J.S. Cho, Y.J. Hong, Y.C. Kang, Electrochemical properties of fiber-in-tube-and filled-structured TiO2 nanofiber anode materials for lithium-ion batteries, Chem. Eur. J. 21 (2015) 11082–11087, https://doi.org/10.1002/chem.201500729.
[4] Y. Pan, Y. Li, J. Song, Y. Xiang, Z. Sui, Q. Tian, Co3O4 nanoparticles anchored on stable Na2Ti2O5 nanobelts for improved lithium storage, Appl. Surf. Sci. 601 (2022), 154273, https://doi.org/10.1016/j.apsusc.2022.154273.
[5] S.B. Patil, H. Phattepur, B. Kishore, R. Viswanatha, G. Nagaraju, Robust electrochemistry of black TiO2 as stable and high-rate negative electrode for lithium-ion batteries, Mater. Renew. Sustain.Energy 8 (2019) 1–10, https://doi.org/10.1007/s40243-019-0147-y.
[6] Q.N. Tran, I.T. Kim, J. Hur, J.H. Kim, H.W. Choi, S.J. Park, Composite of nanocrystalline cellulose with tin dioxide as lightweight substrates for high-performance lithium-ion battery, Korean J. Chem. Eng. 37 (2020) 898–904, https://doi.org/10.1007/s11814-020-0506-5.
[7] L. Shen, C. Xu, J. Gao, J. Tao, Q. Zhang, Y. Chen, Y. Lin, Z. Huang, J. Li, Scalable synthesized high-performance TiO2-Si-C hybrid anode for lithium batteries, J. Energy Chem. 77 (2023) 348–358, https://doi.org/10.1016/j.jechem.2022.10.044.
[8] Q. Tian, Y. Chen, F. Zhang, W. Zhang, Z. Sui, L. Yang, Hierarchical carbon-riveted 2D@0D TiO2 nanosheets@SnO2 nanoparticles composite for a improved lithium-ion battery anode, Appl. Surf. Sci. 511 (2020), 145625, https://doi.org/10.1016/j.apsusc.2020.145625.
[9] S. Luo, T. Yuan, L. Soule, J. Ruan, Y. Zhao, D. Sun, J. Yang, M. Liu, S. Zheng, Enhanced ionic/electronic transport in nano-TiO2/sheared CNT composite electrode for Na+ insertion-based hybrid ion-capacitors, Adv. Funct. Mater. 30 (2020), 1908309, https://doi.org/10.1002/adfm.201908309.
[10] S. Luo, P. Zhang, T. Yuan, J. Ruan, C. Peng, Y. Pang, H. Sun, J. Yang, S. Zheng, Molecular self-assembly of a nanorod N-Li4Ti5O12/TiO2/C anode for superior lithium ion storage, J. Mater. Chem. A 6 (2018) 15755–15761, https://doi.org/10.1039/C8TA05860A.
[11] T. Yuan, L. Soule, B. Zhao, J. Zou, J. Yang, M. Liu, S. Zheng, Recent advances in titanium niobium oxide anodes for high-power lithium-ion batteries, Energy Fuel 34 (2020) 13321–13334, https://doi.org/10.1021/acs.energyfuels.0c02732.
[12] M.S. Jo, G.D. Park, Y.C. Kang, J.S. Cho, Design and synthesis of interconnected hierarchically porous anatase titanium dioxide nanofibers as high-rate and long-cycle-life anodes for lithium-ion batteries, Nanoscale 10 (2018) 13539–13547, https://doi.org/10.1039/C8NR01666F.
[13] J.H. Lee, H.M. Lee, S. Ahn, Battery dimensional changes occurring during charge/discharge cycles—thin rectangular lithium ion and polymer cells, J. Power Sources 119–121 (2003) 833–837, https://doi.org/10.1016/S0378-7753(03)00281-7.
[14] Y. Qi, L.G. Hector, C. James, K.J. Kim, Lithium concentration dependent elastic properties of battery electrode materials from first principles calculations, J. Electrochem. Soc. 161 (2014), F3010, https://doi.org/10.1149/2.0031411jes.
[15] D.P. Opra, S.V. Gnedenkov, S.L. Sinebryukhov, Recent efforts in design of TiO2(B) anodes for high-rate lithium-ion batteries: a review, J. Power Sources 442 (2019), 227225, https://doi.org/10.1016/j.jpowsour.2019.227225.
[16] R. Saroha, A.K. Panwar, A.R. Farooq, L. Krishniya, P. Tyagi, Synthesis and electrochemical characterization of graphene nanoflakes and LiFe0.97Ni0.03PO4/C for lithium-ion battery, Ionics 23 (2017) 2641–2650, https://doi.org/10.1007/s11581-017-2000-6.
[17] R. Saroha, J.-H. Ahn, J.S. Cho, A short review on dissolved lithium polysulfide catholytes for advanced lithium-sulfur batteries, Korean J. Chem. Eng. 38 (2021) 461–474, https://doi.org/10.1007/s11814-020-0729-5.
[18] X. Yan, Z. Wang, M. He, Z. Hou, T. Xia, G. Liu, X. Chen, TiO2 nanomaterials as anode materials for lithium-ion rechargeable batteries, Energy Technol. 3 (2015) 801–814, https://doi.org/10.1002/ente.201500039.
[19] M. Holzapfel, F. Alloin, R. Yazami, Calorimetric investigation of the reactivity of the passivation film on lithiated graphite at elevated temperatures, Electrochim. Acta 49 (2004) 581–589, https://doi.org/10.1016/j.electacta.2003.09.012.
[20] Z. Chen, Y. Gao, Q. Zhang, L. Li, P. Ma, B. Xing, J. Cao, G. Sun, H. Bala, C. Zhang, TiO2/NiO/reduced graphene oxide nanocomposites as anode materials for high-performance lithium ion batteries, J. Alloys Compd. 774 (2019) 873–878, https://doi.org/10.1016/j.jallcom.2018.10.010.
[21] H. Zhou, P. Lv, X. Xia, J. Zhang, J. Yu, Z. Pang, H. Qiao, Q. Wei, MoS2 nanograins doped TiO2 nanofibers as intensified anodes for lithium ion batteries, Mater. Lett. 218 (2018) 47–51, https://doi.org/10.1016/j.matlet.2018.01.149.
[22] W.-H. Ryu, D.-H. Nam, Y.-S. Ko, R.-H. Kim, H.-S. Kwon, Electrochemical performance of a smooth and highly ordered TiO2 nanotube electrode for Li-ion batteries, Electrochim. Acta 61 (2012) 19–24, https://doi.org/10.1016/j.electacta.2011.11.042.
[23] L. Zuniga, V. Agubra, D. Flores, H. Campos, J. Villareal, M. Alcoutlabi, Multichannel hollow structure for improved electrochemical performance of TiO2/Carbon composite nanofibers as anodes for lithium ion batteries, J. Alloys Compd. 686 (2016) 733–743, https://doi.org/10.1016/j.jallcom.2016.06.089.
[24] G. Armstrong, A.R. Armstrong, P.G. Bruce, P. Reale, B. Scrosati, TiO2 (B) nanowires as an improved anode material for lithium-ion batteries containing LiFePO4 or LiNi0.5Mn1.5O4 cathodes and a polymer electrolyte, Adv. Mater. 18 (2006) 2597–2600, https://doi.org/10.1002/adma.200601232.
[25] B.-L. He, B. Dong, H.-L. Li, Preparation and electrochemical properties of Ag-modified TiO2 nanotube anode material for lithium–ion battery, Electrochem. Commun. 9 (2007) 425–430, https://doi.org/10.1016/j.elecom.2006.10.008.

[26] J.-H. Jeong, D.-W. Jung, E.W. Shin, E.-S. Oh, Boron-doped TiO2 anode materials for high-rate lithium ion batteries, J. Alloys Compd. 604 (2014) 226–232, https://doi.org/10.1016/j.jallcom.2014.03.069.
[27] H. Usui, S. Yoshioka, K. Wasada, M. Shimizu, H. Sakaguchi, Nb-doped rutile TiO2: a potential anode material for Na-ion battery, ACS Appl. Mater. Interfaces 7 (2015) 6567–6573, https://doi.org/10.1021/am508670z.
[28] D. Su, S. Dou, G. Wang, Anatase TiO2: better anode material than amorphous and rutile phases of TiO2 for Na-ion batteries, Chem. Mater. 27 (2015) 6022–6029, https://doi.org/10.1021/acs.chemmater.5b02348.
[29] M. Pfanzelt, P. Kubiak, M. Fleischhammer, M. Wohlfahrt-Mehrens, TiO2 rutile—an alternative anode material for safe lithium-ion batteries, J. Power Sources 196 (2011) 6815–6821, https://doi.org/10.1016/j.jpowsour.2010.09.109.
[30] H. He, Q. Gan, H. Wang, G.-L. Xu, X. Zhang, D. Huang, F. Fu, Y. Tang, K. Amine, M. Shao, Structure-dependent performance of TiO2/C as anode material for Na-ion batteries, Nano Energy 44 (2018) 217–227, https://doi.org/10.1016/j.nanoen.2017.11.077.
[31] Z. Yang, G. Du, Q. Meng, Z. Guo, X. Yu, Z. Chen, T. Guo, R. Zeng, Synthesis of uniform TiO2@carbon composite nanofibers as anode for lithium ion batteries with enhanced electrochemical performance, J. Mater. Chem. 22 (2012) 5848–5854, https://doi.org/10.1039/C2JM14852H.
[32] A. Nulu, V. Nulu, K.Y. Sohn, Silicon and porous MWCNT composite as high capacity anode for lithium-ion batteries, Korean J. Chem. Eng. 37 (2020) 1795–1802, https://doi.org/10.1007/s11814-020-0559-5.
[33] Q. Liu, Q. Cao, H. Bi, C. Liang, K. Yuan, W. She, Y. Yang, R. Che, CoNi@ SiO2@ TiO2 and CoNi@Air@TiO2 microspheres with strong wideband microwave absorption, Adv. Mater. 28 (2016) 486–490, https://doi.org/10.1002/adma.201503149.
[34] Y. Chen, W. Huang, D. He, Y. Situ, H. Huang, Construction of heterostructured g-C3N4/Ag/TiO2 microspheres with enhanced photocatalysis performance under visible-light irradiation, ACS Appl. Mater. Interfaces 6 (2014) 14405–14414, https://doi.org/10.1021/am503674e.
[35] X. Li, X. Li, J. Wang, S. Lin, Highly sensitive and selective room-temperature formaldehyde sensors using hollow TiO2 microspheres, Sensors Actuators B Chem. 219 (2015) 158–163, https://doi.org/10.1016/j.snb.2015.05.031.
[36] H. Ren, R. Yu, J. Wang, Q. Jin, M. Yang, D. Mao, D. Kisailus, H. Zhao, D. Wang, Multishelled TiO2 hollow microspheres as anodes with superior reversible capacity for lithium ion batteries, Nano Lett. 14 (2014) 6679–6684, https://doi.org/10.1021/nl503378a.
[37] C. Lai, H. Zhang, G. Li, X. Gao, Mesoporous polyaniline/TiO2 microspheres with core–shell structure as anode materials for lithium ion battery, J. Power Sources 196 (2011) 4735–4740, https://doi.org/10.1016/j.jpowsour.2011.01.077.
[38] J.S. Lee, M.S. Jo, R. Saroha, D.S. Jung, Y.H. Seon, J.S. Lee, Y.C. Kang, D.W. Kang, J. S. Cho, Hierarchically well-developed porous graphene nanofibers comprising N-doped graphitic C-coated cobalt oxide hollow nanospheres as anodes for high-rate Li-ion batteries, Small 16 (2020), 2002213, https://doi.org/10.1002/smll.202002213.
[39] J.S. Lee, R. Saroha, S.H. Oh, D.H. Shin, S.M. Jeong, J.K. Kim, J.S. Cho, Rational design of perforated bimetallic (Ni, Mo) sulfides/N-doped graphitic carbon composite microspheres as anode materials for superior Na-ion batteries, Small Methods 5 (2021), 2100195, https://doi.org/10.1002/smtd.202100195.
[40] W. Wang, Q. Sa, J. Chen, Y. Wang, H. Jung, Y. Yin, Porous TiO2/C nanocomposite shells as a high-performance anode material for lithium-ion batteries, ACS Appl. Mater. Interfaces 5 (2013) 6478–6483, https://doi.org/10.1021/am402350n.
[41] M.S. Jo, S. Ghosh, S.M. Jeong, Y.C. Kang, J.S. Cho, Coral-like yolk–shell-structured nickel oxide/carbon composite microspheres for high-performance Li-ion storage anodes, Nano-Micro Lett. 11 (2019) 1–18, https://doi.org/10.1007/s40820-018-0234-0.
[42] J. Hu, H. Li, X. Huang, Influence of micropore structure on Li-storage capacity in hard carbon spherules, Solid State Ionics 176 (2005) 1151–1159, https://doi.org/10.1016/j.ssi.2005.02.002.
[43] Y.H. Seon, R. Saroha, J.S. Cho, Hierarchically porous N-doped C nanofibers comprising TiO2 quantum dots and ZIF-8-derived hollow C nanocages as ultralight interlayer for stable Li–S batteries, Compos. B Eng. 237 (2022), 109856, https://doi.org/10.1016/j.compositesb.2022.109856.
[44] S.H. Choi, Y.C. Kang, Uniform decoration of vanadium oxide nanocrystals on reduced graphene-oxide balls by an aerosol process for lithium-ion battery cathode material, Chem. Eur. J 20 (2014) 6294–6299, https://doi.org/10.1002/chem.201400134.
[45] S.H. Choi, Y.C. Kang, Y.J. Choi, Y.S. Kim, Superior supercapacitor properties of composite powders with amorphous NiO nanoclusters distributed uniformly in an amorphous carbon matrix, Chem. Asian J. 9 (2014) 2453–2457, https://doi.org/10.1002/asia.201402218.
[46] R. Saroha, A.K. Panwar, Effect of in situ pyrolysis of acetylene (C2H2) gas as a carbon source on the electrochemical performance of LiFePO4 for rechargeable lithium-ion batteries, J. Phys. D. Appl. Phys. 50 (2017), 255501, https://doi.org/10.1088/1361-6463/aa708c.
[47] N. Kitchamsetti, R.S. Kalubarme, P.R. Chikate, C.J. Park, Y.R. Ma, P.M. Shirage, R. S. Devan, An investigation on the effect of Li–ion cycling on the vertically aligned brookite TiO2 nanostructure, ChemistrySelect 4 (2019) 6620–6626, https://doi.org/10.1002/slct.201900395.
[48] W. Xie, R. Li, Q. Xu, Enhanced photocatalytic activity of Se-doped TiO2 under visible light irradiation, Sci. Rep. 8 (2018) 1–10, https://doi.org/10.1038/s41598-018-27135-4.
[49] Q. Wang, D. Xie, J. Chen, G. Liu, M. Yu, Superhydrophobic paper fabricated via nanostructured titanium dioxide-functionalized wood cellulose fibers, J. Mater. Sci. 55 (2020) 7084–7094, https://doi.org/10.1007/s10853-020-04489-7.
[50] S. Gong, Z. Jiang, S. Zhu, J. Fan, Q. Xu, Y. Min, The synthesis of graphene-TiO2/g-C3N4 super-thin heterojunctions with enhanced visible-light photocatalytic activities, J. Nanopart. Res. 20 (2018) 1–13, https://doi.org/10.1007/s11051-018-4399-8.
[51] J.S. Lee, R. Saroha, J.H. Oh, C. Cho, B. Jin, D.-W. Kang, J.S. Cho, Camphene-derived hollow and porous nanofibers decorated with hollow NiO nanospheres and graphitic carbon as anodes for efficient lithium-ion storage, J. Ind. Eng. Chem. 114 (2022) 276–287, https://doi.org/10.1016/j.jiec.2022.07.017.
[52] J.S. Lee, R. Saroha, J.S. Cho, Porous microspheres comprising CoSe2 nanorods coated with N-doped graphitic C and polydopamine-derived C as anodes for long-lived Na-ion batteries, Nano-Micro Lett. 14 (2022) 1–22, https://doi.org/10.1007/s40820-022-00855-z.
[53] S.H. Oh, S.M. Park, D.-W. Kang, Y.C. Kang, J.S. Cho, Fibrous network of highly integrated carbon nanotubes/MoO3 composite bundles anchored with MoO3 nanoplates for superior lithium ion battery anodes, J. Ind. Eng. Chem. 83 (2020) 438–448, https://doi.org/10.1016/j.jiec.2019.12.017.
[54] R. Saroha, H.S. Ka, J.S. Cho, A novel three-dimensional ordered mesoporous microspheres comprising N-doped graphitic carbon-coated FexP nanoparticles as multifunctional interlayers to suppress polysulfide crossover in Li–S batteries, Appl. Surf. Sci. 612 (2023), 155892, https://doi.org/10.1016/j.apsusc.2022.155892.
[55] C.S. Kim, R. Saroha, H.H. Choi, J.H. Oh, G.D. Park, D.-W. Kang, J.S. Cho, High-performance cathode promoted by reduced graphene oxide nanofibers with well-defined interconnected meso-/micro pores for rechargeable Li-Se batteries, J. Ind. Eng. Chem. (2023), https://doi.org/10.1016/j.jiec.2023.02.004.
[56] J.S. Lee, J.-S. Park, K.W. Baek, R. Saroha, S.H. Yang, Y.C. Kang, J.S. Cho, Coral-like porous microspheres comprising polydopamine-derived N-doped C-coated MoSe2 nanosheets composited with graphitic carbon as anodes for high-rate sodium- and potassium-ion batteries, Chem. Eng. J. 456 (2023), 141118, https://doi.org/10.1016/j.cej.2022.141118.
[57] R. Saroha, Y.H. Seon, B. Jin, Y.C. Kang, D.-W. Kang, S.M. Jeong, J.S. Cho, Self-supported hierarchically porous 3D carbon nanofiber network comprising Ni/Co/NiCo2O4 nanocrystals and hollow N-doped C nanocages as sulfur host for highly reversible Li–S batteries, Chem. Eng. J. 446 (2022), 137141, https://doi.org/10.1016/j.cej.2022.137141.
[58] C.S. Kim, J.S. Lee, R. Saroha, Y.B. Park, Y. Chan Kang, D.-W. Kang, S.M. Jeong, J. S. Cho, Porous nitrogen-doped graphene nanofibers comprising metal organic framework-derived hollow and ultrafine layered double metal oxide nanocrystals as high-performance anodes for lithium-ion batteries, J. Power Sources 523 (2022), 231030, https://doi.org/10.1016/j.jpowsour.2022.231030.
[59] J.M. Choi, R. Saroha, J.S. Kim, M.R. Jang, J.S. Cho, Porous nanofibers comprising VN nanodots and densified N-doped CNTs as redox-active interlayers for Li–S batteries, J. Power Sources 559 (2023), 232632, https://doi.org/10.1016/j.jpowsour.2023.232632.
[60] R. Saroha, J.S. Cho, Nanofibers comprising interconnected chain-like hollow N-doped C nanocages as 3D free-standing cathodes for Li–S batteries with super-high sulfur content and lean electrolyte/sulfur ratio, Small Methods 6 (2022), 2200049, https://doi.org/10.1002/smtd.202200049.
[61] R. Saroha, J.H. Oh, Y.H. Seon, Y.C. Kang, J.S. Lee, J.S. Cho, Freestanding interlayers for Li-S batteries: design and synthesis of hierarchically porous N-doped C nanofibers comprising vanadium nitride quantum dots and MOF-derived hollow N-doped C nanocages, J. Mater. Chem. A 9 (2021) 11651–11664, https://doi.org/10.1039/D1TA01802G.
[62] R. Saroha, J. Heo, Y. Liu, N. Angulakshmi, Y. Lee, K.-K. Cho, H.-J. Ahn, J.-H. Ahn, V2O3-decorated carbon nanofibers as a robust interlayer for long-lived, high-performance, room-temperature sodium–sulfur batteries, Chem. Eng. J. 431 (2022), 134205, https://doi.org/10.1016/j.cej.2021.134205.
[63] R. Saroha, J.H. Oh, J.S. Lee, Y.C. Kang, S.M. Jeong, D.-W. Kang, C. Cho, J.S. Cho, Hierarchically porous nanofibers comprising multiple core–shell Co3O4@graphitic carbon nanoparticles grafted within N-doped CNTs as functional interlayers for excellent Li–S batteries, Chem. Eng. J. 426 (2021), 130805, https://doi.org/10.1016/j.cej.2021.130805.
[64] J. Li, J. Huang, J. Li, L. Cao, H. Qi, Y. Cheng, Q. Xi, H. Dang, Improved Li-ion diffusion process in TiO2/rGO anode for lithium-ion battery, J. Alloys Compd. 727 (2017) 998–1005, https://doi.org/10.1016/j.jallcom.2017.08.121.
[65] M. Han, J. Li, J. Yu, Microspheres integrating Ti2O3 nanocrystals, carbon matrix, and vertical graphene enable fast ion transport for fast-charging lithium-ion batteries, J. Energy Storage 43 (2021), 103179, https://doi.org/10.1016/j.est.2021.103179.
[66] G. Xu, J. Han, B. Ding, P. Nie, J. Pan, H. Dou, H. Li, X. Zhang, Biomass-derived porous carbon materials with sulfur and nitrogen dual-doping for energy storage, Green Chem. 17 (2015) 1668, https://doi.org/10.1039/c4gc02185a.
[67] M.S. Jo, J.S. Lee, S.Y. Jeong, J.K. Kim, Y.C. Kang, D.W. Kang, S.M. Jeong, J.S. Cho, Golden bristlegrass-like hierarchical graphene nanofibers entangled with N-doped CNTs containing CoSe2 nanocrystals at each node as anodes for high-rate sodium-ion batteries, Small 16 (2020), 2003391, https://doi.org/10.1002/smll.202003391.
[68] J.M. Choi, J.S. Lee, J.S. Cho, One-pot synthesis strategy of sea urchin-like hollow microspheres comprising MoOx nanorods attached via N-doped C as anodes for lithium-ion batteries, Chem. Eng. J. 439 (2022), 135536, https://doi.org/10.1016/j.cej.2022.135536.
[69] S.Y. Jeong, J.S. Cho, Porous hybrid nanofibers comprising ZnSe/$CoSe_2$/carbon with uniformly distributed pores as anodes for high-performance sodium-ion batteries, Nanomaterials 9 (2019) 1362, https://doi.org/10.3390/nano9101362.
[70] R. Saroha, A. Gupta, A.K. Panwar, Electrochemical performances of Li-rich layered-layered Li2MnO3-LiMnO2 solid solutions as cathode material for lithium-ion

batteries, J. Alloys Compd. 696 (2017) 580–589, https://doi.org/10.1016/j.jallcom.2016.11.199.
[71] R. Saroha, A.K. Panwar, Y. Sharma, P.K. Tyagi, S. Ghosh, Development of surface functionalized ZnO-doped LiFePO4/C composites as alternative cathode material for lithium ion batteries, Appl. Surf. Sci. 394 (2017) 25–36, https://doi.org/10.1016/j.apsusc.2016.09.105.
[72] R. Saroha, A.K. Panwar, Y. Sharma, Physicochemical and electrochemical performance of LiFe1−xNixPO4 ($0 \leq x \leq 1.0$) solid solution as potential cathode material for rechargeable lithium-ion battery, Ceram. Int. 43 (2017) 5734–5742, https://doi.org/10.1016/j.ceramint.2017.01.115.